nature nanotechnology

LETTERS

https://doi.org/10.1038/s41565-018-0221-0

Lifetime-engineered NIR-II nanoparticles unlock multiplexed in vivo imaging

Yong Fan[1], Peiyuan Wang[1], Yiqing Lu[2]*, Rui Wang[1], Lei Zhou[1], Xianlin Zheng[2], Xiaomin Li[1], James A. Piper[2] and Fan Zhang[1]*

Deep tissue imaging in the second near-infrared (NIR-II) window holds great promise for physiological studies and biomedical applications[1–6]. However, inhomogeneous signal attenuation in biological matter[7,8] hampers the application of multiple-wavelength NIR-II probes to multiplexed imaging. Here, we present lanthanide-doped NIR-II nanoparticles with engineered luminescence lifetimes for in vivo quantitative imaging using time-domain multiplexing. To achieve this, we have devised a systematic approach based on controlled energy relay that creates a tunable lifetime range spanning three orders of magnitude with a single emission band. We consistently resolve selected lifetimes from the NIR-II nanoparticle probes at depths of up to 8 mm in biological tissues, where the signal-to-noise ratio derived from intensity measurements drops below 1.5. We demonstrate that robust lifetime coding is independent of tissue penetration depth, and we apply in vivo multiplexing to identify tumour subtypes in living mice. Our results correlate well with standard ex vivo immunohistochemistry assays, suggesting that luminescence lifetime imaging could be used as a minimally invasive approach for disease diagnosis.

Fluorescence imaging is extensively used in life sciences because of its ability to carry out multi-channel (multi-colour) observations with high sensitivity and high spatio-temporal resolution[9–11]. In the past few years, significant efforts have been made to produce fluorescent probes that operate in the second near-infrared (NIR-II) window (1.0–1.7 μm), which offers enhanced penetration into biological tissues[1–6,12–17]. These probes have shown significant potential for real-time investigations of live biological and physiological processes as well as clinical applications ranging from non-invasive diagnosis to image-guided surgery. Conventional fluorescence techniques using different colours to simultaneously examine different analytes have been shown to be applicable in a variety of in vitro diagnostics, but such spectral multiplexing is generally impractical in vivo. This is especially true for deep tissue imaging, where the different absorption and scattering spectra of the complex tissue structures (including skin, muscle, fat, bone and body fluids) present serious difficulties for spectral multiplexing[7,8]. As the biological composition varies from location to location and cannot be determined exactly a priori, quantitative multiplexing that takes into account the influence of this heterogeneity on different wavelengths remains impractical. So far, in vivo NIR-II imaging has largely been limited to a single probe[2,6,13,16], or very occasionally to two probes at a time, with little assessment of their quantitative accuracy[4,14].

To address this challenge, we turned to the temporal domain. Specifically we have devised a luminescence lifetime detection/imaging approach based on lanthanide-doped NIR-II nanoparticles synthesized with selectable luminescence lifetimes (τ) that span the microsecond to millisecond region. Employing Nd^{3+} sensitizers and either Er^{3+} or Ho^{3+} emitters, these nanoparticles absorb 808 nm excitation and emit luminescence centred at 1,525 and 1,155 nm, respectively (Fig. 1a). A series of lifetime populations are produced for each emission band (Supplementary Sections 1 and 2), with each sample filled into an individual capillary (~0.46 mM) for both ordinary imaging and lifetime imaging using a purpose-built system (Supplementary Section 3). Intralipid medium (1%) and a set of bovine bones with increasing thickness were used to simulate attenuation by biological tissues, which affects both the effective excitation and the luminescence signal.

As shown in Fig. 1b, for ordinary intensity-based imaging, the visibility of the capillaries deteriorated as the immersion depth of the Intralipid or the thickness of the bone increased. The Er^{3+} emission decreased more rapidly due to the water absorption peak around 1,450 nm, whereas the Ho^{3+} emission underwent stronger scattering because of the shorter wavelength. Furthermore, though the intensities decreased exponentially with respect to the immersion depth in the homogeneous Intralipid medium, as expected by the Beer–Lambert law, under bones the attenuation of luminescence was irregular and unpredictable due to the varied composition of the bones collected (Fig. 1c). By contrast, luminescence lifetime imaging clearly recognized the capillaries against the background, with the consistent pseudo-colours indicating the high reliability of the lifetime measurement, even where the signal-to-noise ratio of the intensity measurement dropped to a very low level (1.46 at 8 mm compared to 47.1 at 0 mm for Er-τ5 nanoparticles; Supplementary Fig. 8). For all nanoparticle samples imaged, the relative change in the mean lifetime values was within 11.8% (Fig. 1c). The coefficient of variation (CV) of the lifetimes increased from 3.1% (at 0 mm) to 12.9% (at 8 mm) with respect to the penetration depth, mainly due to uncertainty in the lifetime computation caused by the reduced signal-to-noise ratios.

To create lifetime-engineered NIR-II nanoparticles we designed a systematic approach based on controlled energy relay in a core–multi-shell nanostructure. As shown in Fig. 2a, the example nanoparticle consists of an outer layer co-doped with Nd^{3+} and Yb^{3+}, an intermediate layer doped with Yb^{3+} only, and an inner layer co-doped with Yb^{3+} and Er^{3+}. With 808 nm illumination, the Nd^{3+} sensitizers confined in the outer layer harvest the excitation photons, and transfer the energy to the Yb^{3+} ions in the same layer via inter-ionic

[1]Department of Chemistry, State Key Laboratory of Molecular Engineering of Polymers, Shanghai Key Laboratory of Molecular Catalysis and Innovative Materials and iChem, Fudan University, Shanghai, China. [2]ARC Centre of Excellence for Nanoscale BioPhotonics (CNBP), Department of Physics and Astronomy, Macquarie University, Sydney, New South Wales, Australia. *e-mail: yiqing.lu@mq.edu.au; zhang_fan@fudan.edu.cn

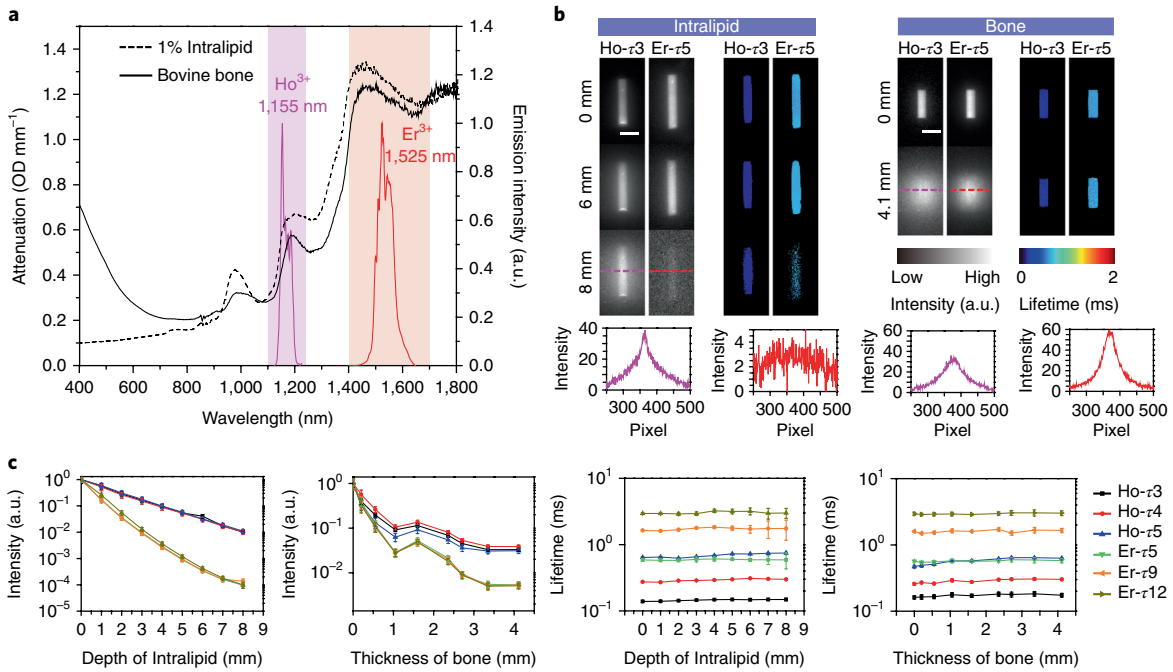

Fig. 1 | Comparison between spectral and lifetime channels for deep tissue imaging. a, Attenuation spectra (left axis) of 1% Intralipid and a 4.1 mm sample of bovine bone, alongside the NIR-II emission bands (right axis) of Ho and Er nanoparticles. Colour shades correspond to the spectral ranges for collecting respective emissions. OD, optical density. **b**, Ordinary intensity-based images and luminescence lifetime images of capillaries containing Ho-τ3 and Er-τ5 nanoparticles before and after being covered by Intralipid or bone. The colour (hue) of each pixel in the lifetime images represents its lifetime value. Profiles underneath correspond to horizontal dashed lines in the intensity images. Scale bars, 2 mm. **c**, Normalized intensities (left two plots) and lifetimes (right two plots) obtained for Ho and Er nanoparticles with respect to immersion depth of the Intralipid solution and thickness of the bone. Each data and error bar represents mean ± s.d. for every pixel of the capillary in the corresponding intensity/lifetime image. Details of nanoparticles and experimental parameters used for lifetime imaging are summarized in Supplementary Tables 1–4.

cross-relaxation. The energy is then relayed via diffusive energy migration among the Yb^{3+} sublattice, until reaching the inner layer, where it is entrapped by the Er^{3+} emitters to generate luminescence at 1,525 nm. This structure allows the luminescence lifetime to be tuned systematically in both directions. On the one hand, increasing the thickness of the energy relay layer prolongs the average process from absorption to emission, leading to a longer lifetime. On the other hand, at a defined thickness of the energy relay layer corresponding to identical capacity of the Yb^{3+} sublattice, an increase in the Er^{3+} concentration accelerates the conversion of stored energy into luminescence emission, which shortens the lifetime.

A series of the core–multi-shell nanoparticles were fabricated in the general form of hexagonal (β) phase $NaGdF_4$@$NaGdF_4$:Yb,Er@$NaYF_4$:Yb@$NaNdF_4$:Yb (Fig. 2b). The $NaGdF_4$ inert core was used to facilitate uniform epitaxial growth of the shells in sequential synthesis steps so as to achieve a small final size of around 20 nm. For the group of nanoparticles with all parameters identical other than the increasing thickness of the energy relay layer (d = 0, 0.1, 0.2, 0.9, 2.4 and 3.6 nm), the luminescence lifetime at 1,525 nm was effectively extended from 1.25 ms to 7.21 ms (Fig. 2c). The longest lifetime we achieved was 20.9 ms when increasing the relay layer thickness to 7.0 nm (alongside a thicker activation layer). For the other group, on varying only the Er^{3+} doping in the activation layer (from 2% to 30%; identical energy relay shell thickness of 0.9 nm), the lifetime decreased from 2.75 ms to 292 µs (Fig. 2d). Even shorter lifetimes down to 5.8 µs were demonstrated by removing the energy relay layer entirely and increasing the Er^{3+} doping concentration to 45%. Altogether, a substantial lifetime-selectable range spanning three orders of magnitude was demonstrated for the Er^{3+} 1,525 nm emission (Supplementary Table 1), easily accommodating more than 10 distinct lifetime identities that were clearly distinguished using our time-resolved imaging system (Fig. 2e; very short and very long lifetimes are not included for a better visual effect of the pseudocolour mapping).

As well as for Er^{3+}, tunable lifetimes were achieved for other lanthanide ions emitting in the NIR-II window, including Ho^{3+} at 1,155 nm, Pr^{3+} at 1,289 nm, Tm^{3+} at 1,475 nm as well as Nd^{3+} itself at 1,060 nm (Fig. 3a and Supplementary Section 2). Taking Ho nanoparticles, for example, lifetimes ranging from 40 to 920 µs were generated via the energy relay strategy (Fig. 3b and Supplementary Table 2). These lifetime identities, engineered independently at multiple NIR-II emission bands, enable lifetime-based coding of different information carriers so as to deliver a high level of multiplexing in vivo. To demonstrate this, we encapsulated the as-prepared Er and Ho nanoparticles into polydimethylsiloxane (PDMS) beads of 1 mm in diameter (Supplementary Section 4). Each bead represented a two-digit code, one digit corresponding to the Ho^{3+} luminescence at 1,155 nm and the other to the Er^{3+} emission at 1,525 nm (Fig. 3c). The beads were mixed and placed in a Petri dish covered with phantom tissue (1% Intralipid medium), and lifetime imaging was performed for the two emission bands. As shown in Fig. 3d, consistent lifetime values were obtained for each bead at both wavelengths, regardless of the tissue depth. Assuming that the two lifetimes follow bivariate normal distributions, the 99.9999% confidence regions (corresponding to 1 ppm error rates) of the clustered beads populations are kept far apart from each other, so every single bead can be unambiguously identified by its specific lifetime codes. By contrast, conventional spectral multiplexing relying on ratiometric intensities was unable to distinguish the different populations as the tissue depth increased (Fig. 3e), demonstrating that its application in vivo is restricted to a shallow penetration depth and is therefore of limited practicality.

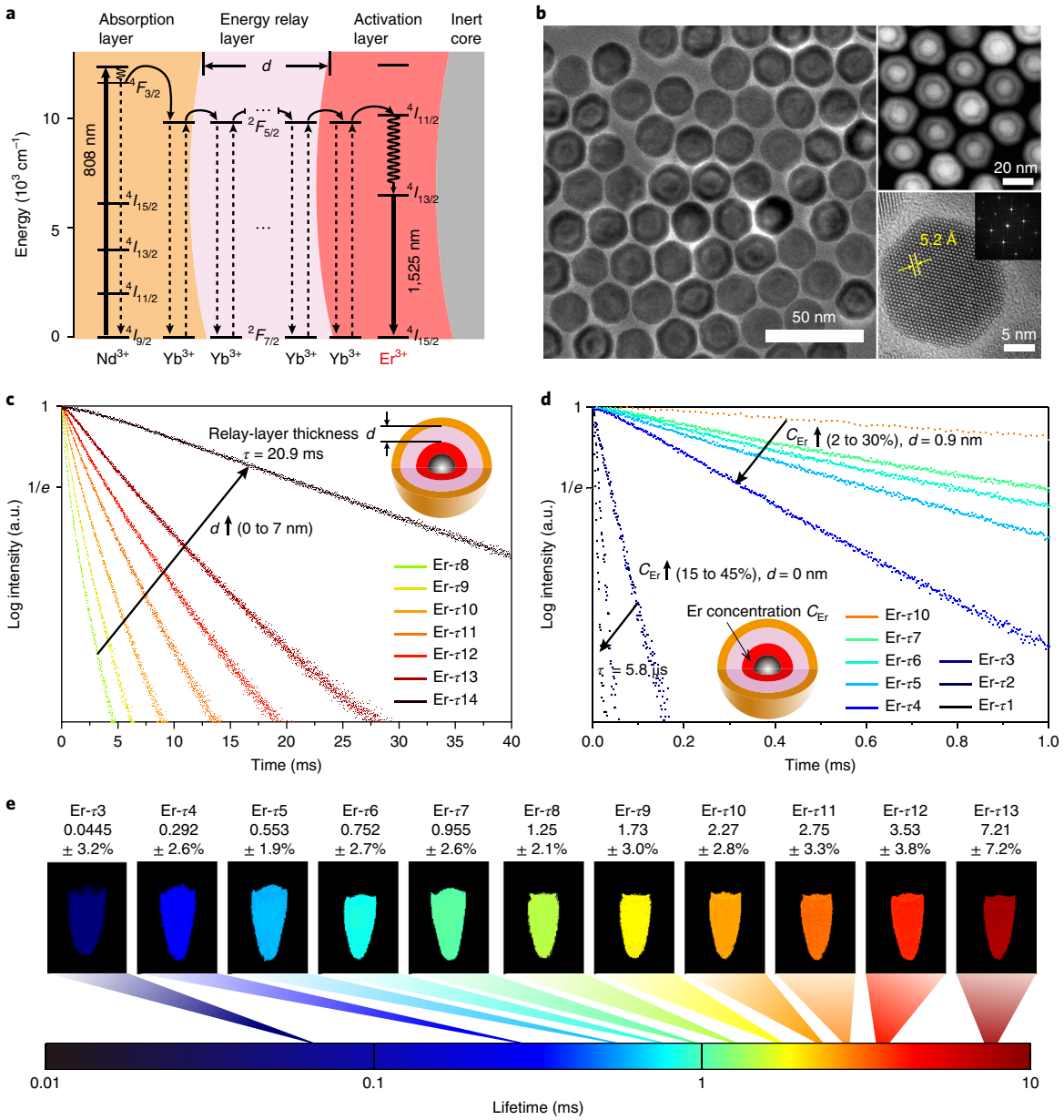

Fig. 2 | Controlled energy relay for lifetime tuning. a, Energy level diagram illustrating the luminescence process of the core–multi-shell nanoparticles. **b**, Transmission electron microscopy (TEM) image (left), high-angle annular dark-field scanning transmission electron microscopy (HAADF-STEM) image (top right), high-resolution (HR) TEM image and the corresponding fast Fourier transform (bottom right) of the Er-τ12 ($NaGdF_4$@$NaGdF_4$:Yb,Er@$NaYF_4$:Yb@$NaNdF_4$:Yb) nanoparticles. **c**, Luminescence decay curves measured at 1,525 nm from the as-prepared Er nanoparticles with energy relay shells of increasing thickness d from 0 to 7 nm (identical composition). **d**, Luminescence decay curves of the nanoparticles with incremental Er^{3+} doping concentration C_{Er} from 2% to 30% for $d = 0.9$ nm and from 15% to 45% for $d = 0$ nm. **e**, Pseudocolour-mapped lifetime images of the Er nanoparticles contained in centrifuge tubes acquired by the time-resolved NIR-II imaging system. All nanoparticles were dispersed in cyclohexane at ~0.46 mM molar concentration. Numbers accompanying each sample indicate mean ± CV of the measured luminescence lifetime, taken from pixels corresponding to each tube in the lifetime images. Details of nanoparticles and experimental parameters used for lifetime imaging are summarized in Supplementary Tables 1 and 5, respectively.

The validated robustness of lifetime multiplexing encouraged us to further explore its potential for cancer diagnostics in vivo. We took nude mice bearing xenografted tumours from either MCF-7 or BT-474 breast cancer cells as a model, with 10 mice per tumour subtype. Three lifetime populations of the Er nanoparticles (Er-τ5, Er-τ9 and Er-τ13) were conjugated with primary antibodies against three routinely examined biomarkers for breast cancer[18,19], oestrogen receptor (ER), progesterone receptor (PR) and human epidermal growth factor receptor-2 (HER2), respectively (Supplementary Section 5). Of the 10 mice of the same tumour subtype, half (the positive group) were intravenously injected with a cocktail of the antibody-conjugated nanoparticles, while the remainder (the control group) were injected with identical populations of nanoparticles with no antibody conjugation but phospholipid coating. Imaging at a series of time points post-injection (Supplementary Section 6) showed that, for both tumour subtypes, the NIR-II luminescence from the tumours remained sufficiently high to distinguish the positive groups, whereas for the control groups the nanoparticles

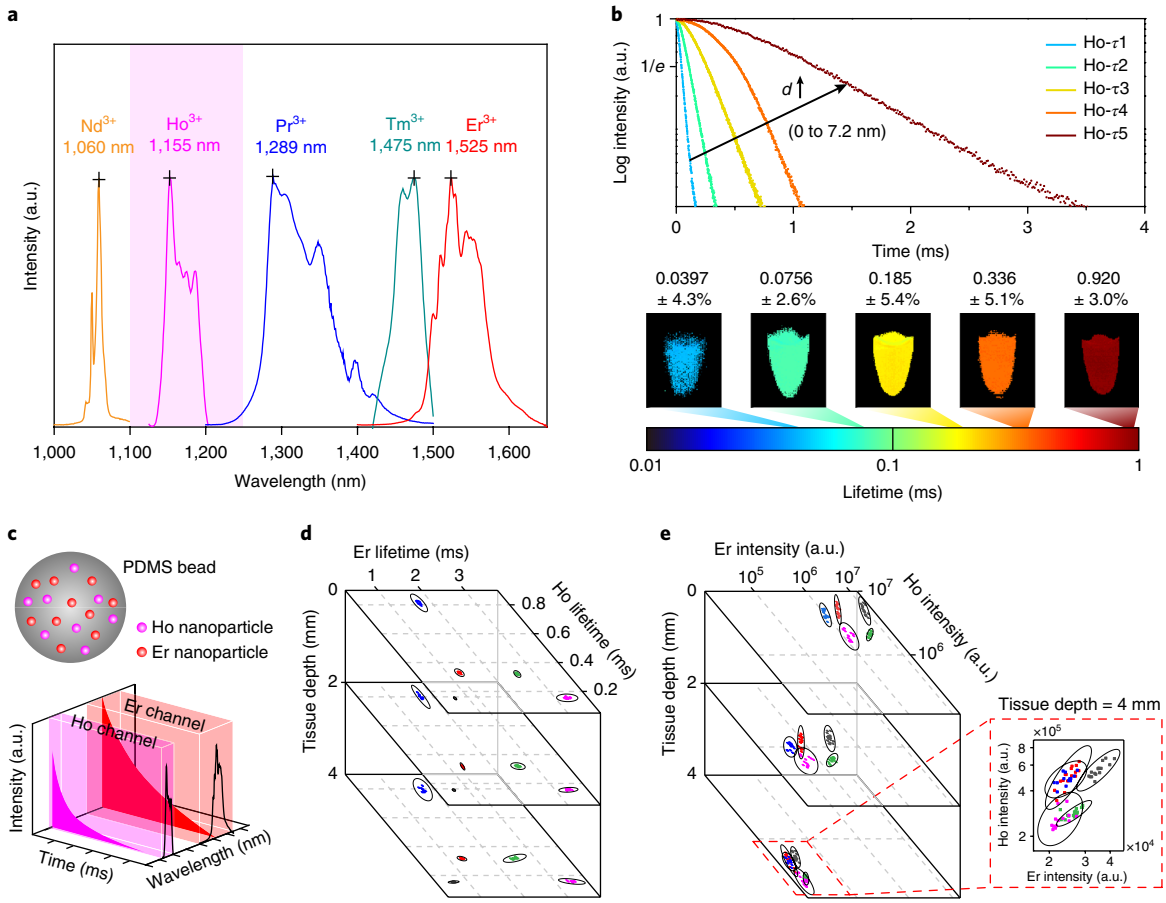

Fig. 3 | Luminescence coding using lifetime-engineered NIR-II nanoparticles a, Available emission bands of trivalent lanthanide ions in the 1,000–1,700 nm region. **b**, Luminescence decay curves (top) and lifetime images (bottom) measured at the 1,155 nm band of Ho-doped core–multi-shell nanoparticles. All nanoparticles were dispersed in cyclohexane at ~0.46 mM molar concentration. Numbers accompanying each sample indicate mean ± CV of the measured luminescence lifetime, taken for pixels corresponding to each tube in the lifetime images. Details of the nanoparticles and experimental parameters used for lifetime imaging are summarized in Supplementary Tables 2 and 6, respectively. **c**, Scheme of two-channel luminescence coding based on PDMS beads encapsulating Ho and Er nanoparticles. **d**,**e**, Scatter plots measured from five batches of beads encoded by lifetimes (**d**) and intensities (**e**) at increased tissue depths (0, 2 and 4 mm). Ellipses around the clusters represent 99.9999% (**d**) and 99% (**e**) confidence regions by fitting bivariate normal distributions. A further explanation for luminescence-lifetime-based coding is provided in the Methods and Supplementary Section 4.

non-specifically accumulated at the tumour site were eventually cleared. This allowed us to quantify the biomarker expressions of the tumour subtypes by resolving the three lifetime components simultaneously using a pattern recognition algorithm[20,21] (Fig. 4a and Supplementary Section 7). Remarkably, despite variation in the overall intensities, which is not surprising given that the tumours as well as tissue attenuation are unlikely to be identical in individual mice, the expression patterns of the three biomarkers are clearly (statistically) different for the two tumour subtypes (Fig. 4b). The MCF-7 tumours expressed a large amount of ER (62.3%) but moderate levels of PR (17.9%) and HER2 (19.8%). On the other hand, the highest expression in the BT-474 tumours came from HER2 (46.6%), followed by PR (28%) and ER (25.4%). These expression patterns acquired by our in vivo multiplexing (IVM) method are highly consistent with the in vitro western blot (WB) results we obtained (Fig. 4c) as well as those in the literature[22,23].

Finally, we compared the IVM method with conventional ex vivo immunohistochemistry (IHC), which nowadays is widely performed for the identification of cancer subtypes using tissue samples collected via biopsy. IHC was carried out using three mice for each tumour subtype (from the same batches as for the imaging studies), and the images were analysed using the IHC Profiler algorithm[24] to quantify the biomarker expression levels as well as to obtain the conventional semi-quantitative scores on a scale of 0, 1+, 2+ and 3+ (Fig. 4d and Supplementary Section 8). Statistically, excellent correlation was found between the two methods for the biomarker expression patterns of both tumour subtypes (Fig. 4d). Nevertheless, for multiple pieces of tissues collected from the same mouse, a high level of heterogeneity was clearly observed among the IHC images staining the same receptor (Supplementary Fig. 19). This reflects the universal concern over the reliability of IHC, with a number of reports suggesting that the outcomes are prone to sample preparation and subjective scoring[25,26], especially given that conventional IHC only examines one biomarker per tissue slide. By contrast, IVM allows all the biomarkers to be quantified simultaneously to minimize uncertainty caused by the biopsy, sample processing and scoring procedures. It also eliminates the risk of tumour cell reseeding following biopsy[27]. Being effectively real-time and minimally invasive, IVM can significantly reduce the time, labour and cost of diagnosing tumour subtypes, critical factors for effective therapeutic decisions and prognosis, and offering a superior alternative to IHC with improved reliability and patient experience.

In summary, this work illustrates the feasibility of engineering NIR-II lanthanide nanoparticles to create distinct lifetime channels for multiplexed in vivo imaging, whereby wavelength-dependent attenuation from different biological substances does not detract

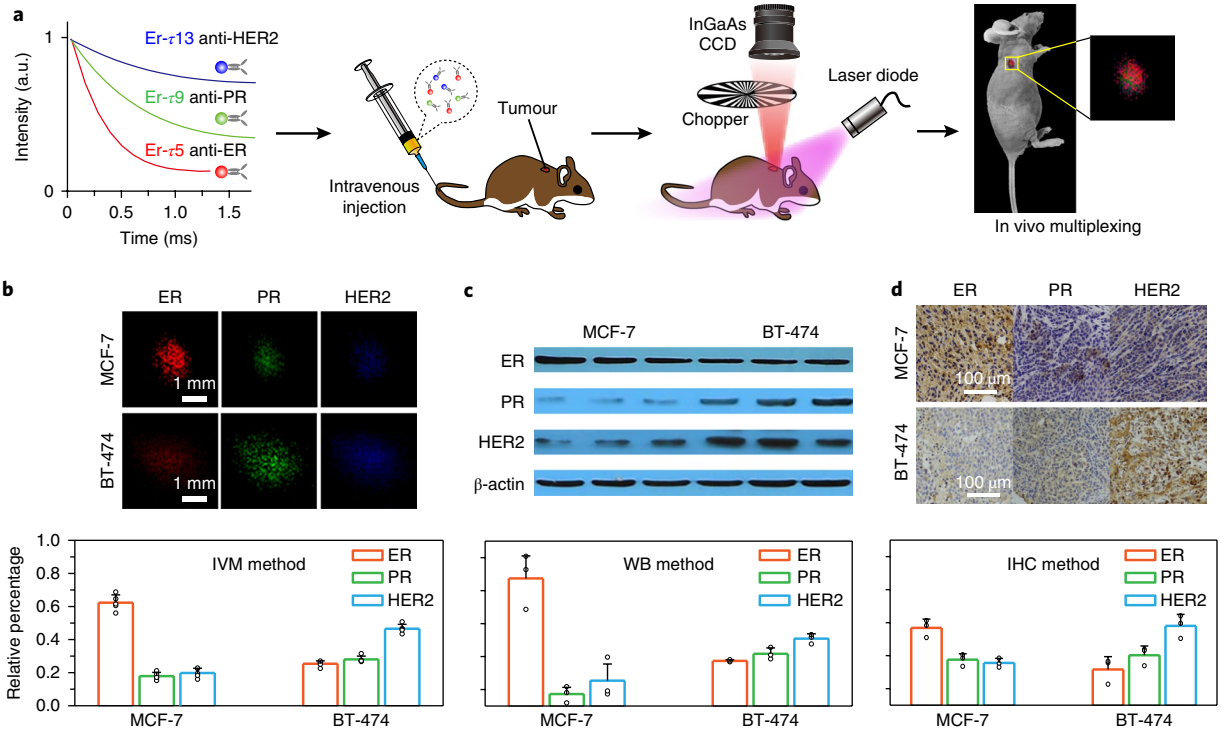

Fig. 4 | Lifetime-resolved imaging for IVM of tumour biomarkers. a, Schematics illustrating animal experiment procedures. Three batches of Er nanoparticles exhibiting distinct lifetimes are conjugated to three antibodies (anti-ER, anti-PR and anti-HER2), respectively, and intravenously injected into the mouse via tail vein. Lifetime-resolved imaging is then performed to quantify the biomarker expressions on the tumour via IVM. CCD, charge-coupled device. **b**, Lifetime-resolved images for the MCF-7 and BT-474 tumours are decomposed into the three lifetime channels, represented by the red, green and blue monochromatic image sets. Biomarker expression patterns are calculated by integrating the intensities of each components, normalized by the total intensity over the entire tumour area. Experimental parameters used for lifetime imaging are summarized in Supplementary Table 9. **c**,**d**, In vitro western blot (**c**) and ex vivo immunohistochemistry assay (**d**) results and calculated biomarker expression patterns of the two tumour subtypes IVM: in vivo multiplexing; WB: western blot; IHC: immunohistochemistry. Error bars in **b**–**d** represent mean ± s.d., with $n = 5$ biologically independent animals in **b** and $n = 3$ biologically independent animals in **c** and **d** (circles are actual data points).

from accurate quantification. The energy relay approach implemented in the core–multi-shell nanostructure facilitates fine tailoring of the luminescence lifetime over a dynamic range as large as three orders of magnitude, so that a matrix comprising 1×10^5 individual time-domain codes can potentially be generated, opening new opportunities for in vivo flow and image cytometry for point-of-care diagnostics[28,29]. Though an imaging depth of ~6–8 mm is demonstrated here, this can be improved by optimization of the nanostructure (Supplementary Section 9) and advanced approaches such as dye sensitization[17] to produce brighter nanoparticles, which will also speed up data acquisition. Additionally, lifetime imaging employing pulsed excitation and delayed detection contributes to providing higher sensitivity and contrast by removing autofluorescence background. The risk of thermal accumulation and damage to the tissue is also reduced comparing to ordinary intensity imaging, rendering the use of high-power lasers less a concern. Because lifetime measurement is immune to the constant background from ambient light, augmented reality can be integrated to enable intraoperative diagnosis and guidance of surgical procedures[30]. Given the low toxicity of lanthanide nanoparticles[31], we believe the technology presented here will be transformational for a wide range of biomedical research and clinical applications.

Methods

Methods, including statements of data availability and any associated accession codes and references, are available at https://doi.org/10.1038/s41565-018-0221-0.

Received: 29 November 2017; Accepted: 4 July 2018;
Published online: 6 August 2018

References

1. Smith, A. M., Mancini, M. C. & Nie, S. Bioimaging: second window for in vivo imaging. *Nat. Nanotech.* **4**, 710–711 (2009).
2. Hong, G. et al. Through-skull fluorescence imaging of the brain in a new near-infrared window. *Nat. Photon.* **8**, 723–730 (2014).
3. Ghosh, D. et al. Deep, noninvasive imaging and surgical guidance of submillimeter tumors using targeted M13-stabilized single-walled carbon nanotubes. *Proc. Natl Acad. Sci. USA* **111**, 13948–13953 (2014).
4. Bruns, O. T. et al. Next-generation in vivo optical imaging with short-wave infrared quantum dots. *Nat. Biomed. Eng.* **1**, 0056 (2017).
5. Wong, M. H. et al. Nitroaromatic detection and infrared communication from wild-type plants using plant nanobionics. *Nat. Mater.* **16**, 264–272 (2017).
6. Sun, Y. et al. Novel bright-emission small-molecule NIR-II fluorophores for in vivo tumor imaging and image-guided surgery. *Chem. Sci.* **8**, 3489–3493 (2017).
7. Jacques, S. L. Optical properties of biological tissues: a review. *Phys. Med. Biol.* **58**, R37–61 (2013).
8. Bashkatov, A. N., Genina, E. A., Kochubey, V. I. & Tuchin, V. V. Optical properties of human skin, subcutaneous and mucous tissues in the wavelength range from 400 to 2000 nm. *J. Phys. D* **38**, 2543–2555 (2005).
9. James, M. L. & Gambhir, S. S. A molecular imaging primer: modalities, imaging agents, and applications. *Physiol. Rev.* **92**, 897–965 (2012).
10. Ntziachristos, V. Going deeper than microscopy: the optical imaging frontier in biology. *Nat. Methods* **7**, 603–614 (2010).
11. Yun, S. H. & Kwok, S. J. J. Light in diagnosis, therapy and surgery. *Nat. Biomed. Eng.* **1**, 0008 (2017).
12. Antaris, A. L. et al. A small-molecule dye for NIR-II imaging. *Nat. Mater.* **15**, 235–242 (2016).

13. Dang, X. et al. Layer-by-layer assembled fluorescent probes in the second near-infrared window for systemic delivery and detection of ovarian cancer. *Proc. Natl Acad. Sci. USA* **113**, 5179–5184 (2016).
14. Naczynski, D. J. et al. Rare-earth-doped biological composites as in vivo shortwave infrared reporters. *Nat. Commun.* **4**, 2199 (2013).
15. Trivedi, E. R. et al. Highly emitting near-infrared lanthanide 'encapsulated sandwich' metallacrown complexes with excitation shifted toward lower energy. *J. Am. Chem. Soc.* **136**, 1526–1534 (2014).
16. Chen, G. et al. Tracking of transplanted human mesenchymal stem cells in living mice using near-infrared Ag_2S quantum dots. *Adv. Funct. Mater.* **24**, 2481–2488 (2014).
17. Shao, W. et al. Tunable narrow band emissions from dye-sensitized core/shell/shell nanocrystals in the second near-infrared biological window. *J. Am. Chem. Soc.* **138**, 16192–16195 (2016).
18. Hammond, M. E. et al. American Society of Clinical Oncology/College of American Pathologists guideline recommendations for immunohistochemical testing of estrogen and progesterone receptors in breast cancer (unabridged version). *Arch. Pathol. Lab. Med.* **134**, e48–72 (2010).
19. Wolff, A. C. et al. Recommendations for human epidermal growth factor receptor 2 testing in breast cancer: American Society of Clinical Oncology/College of American Pathologists clinical practice guideline update. *J. Clin. Oncol.* **31**, 3997–4013 (2013).
20. Lu, Y. et al. On-the-fly decoding luminescence lifetimes in the microsecond region for lanthanide-encoded suspension arrays. *Nat. Commun.* **5**, 3741 (2014).
21. Niehorster, T. et al. Multi-target spectrally resolved fluorescence lifetime imaging microscopy. *Nat. Methods* **13**, 257–262 (2016).
22. Yezhelyev, M. V. et al. In situ molecular profiling of breast cancer biomarkers with multicolor quantum dots. *Adv. Mater.* **19**, 3146–3151 (2007).
23. Zhou, L. et al. Single-band upconversion nanoprobes for multiplexed simultaneous in situ molecular mapping of cancer biomarkers. *Nat. Commun.* **6**, 6938 (2015).
24. Varghese, F. et al. IHC profiler: an open source plugin for the quantitative evaluation and automated scoring of immunohistochemistry images of human tissue samples. *PLoS ONE* **9**, e96801 (2014).
25. Ramos-Vara, J. A. & Miller, M. A. When tissue antigens and antibodies get along: revisiting the technical aspects of immunohistochemistry—the red, brown, and blue technique. *Vet. Pathol.* **51**, 42–87 (2014).
26. Walker, R. A. Quantification of immunohistochemistry—issues concerning methods, utility and semiquantitative assessment I. *Histopathology* **49**, 406–410 (2006).
27. Robertson, E. G. & Baxter, G. Tumour seeding following percutaneous needle biopsy: the real story! *Clin. Radiol.* **66**, 1007–1014 (2011).
28. Georgakoudi, I. et al. In vivo flow cytometry: a new method for enumerating circulating cancer cells. *Cancer Res.* **64**, 5044–5047 (2004).
29. Ming, K. et al. Integrated quantum dot barcode smartphone optical device for wireless multiplexed diagnosis of infected patients. *ACS Nano* **9**, 3060–3074 (2015).
30. Gorpas, D., Ma, D., Bec, J., Yankelevich, D. R. & Marcu, L. Real-time visualization of tissue surface biochemical features derived from fluorescence lifetime measurements. *IEEE Trans. Med. Imaging* **35**, 1802–1811 (2016).
31. Gnach, A., Lipinski, T., Bednarkiewicz, A., Rybka, J. & Capobianco, J. A. Upconverting nanoparticles: assessing the toxicity. *Chem. Soc. Rev.* **44**, 1561–1584 (2015).

Acknowledgements

This work was supported by the National Key R&D Program of China (2017YFA0207303), the National Natural Science Fund for Distinguished Young Scholars (21725502), the Key Basic Research Program of Science and Technology Commission of Shanghai Municipality (17JC1400100), the China Postdoctoral Science Foundation (KLH1615151), the Australian Research Council Discovery Early Career Researcher Award (DE170100821) and the Centre of Excellence for Nanoscale BioPhotonics (CE140100003).

Author contributions

F.Z., Y.F. and Y.L. designed the project. Y.F. and R.W. synthesized the nanoparticles. Y.L., Y.F. and X.Z. built the optical system. P.W. and L.Z. conducted the animal experiments. Y.F. was primarily responsible for data collection. Y.F., Y.L. and F.Z. analysed the results, and prepared the manuscript, figures and Supplementary Information. All authors contributed to the discussion and editing of the manuscript.

Competing interests

The authors declare no competing interests.

Additional information

Supplementary information is available for this paper at https://doi.org/10.1038/s41565-018-0221-0.

Reprints and permissions information is available at www.nature.com/reprints.

Correspondence and requests for materials should be addressed to Y.L. or F.Z.

Publisher's note: Springer Nature remains neutral with regard to jurisdictional claims in published maps and institutional affiliations.

Methods

Chemical reagents. Gadolinium(III) chloride anhydrous ($GdCl_3$, 99.99%), ytterbium(III) chloride anhydrous ($YbCl_3$, 99.9%), yttrium(III) chloride anhydrous (YCl_3, 99.9%), erbium(III) chloride anhydrous ($ErCl_3$, 99.9%), neodymium(III) chloride anhydrous ($NdCl_3$, 99.9%), holmium(III) chloride anhydrous ($HoCl_3$, 99.9%), thulium(III) chloride anhydrous ($TmCl_3$, 99.9%), praseodymium(III) chloride anhydrous ($PrCl_3$, 99.9%), sodium trifluoroacetate (Na-TFA, 98%), oleic acid (90%) and 1-octadecene (ODE, 90%) were purchased from Sigma-Aldrich. Sodium hydroxide (NaOH, 96%) and ammonium fluoride (NH_4F, 96%) were purchased from Beijing Chemical Reagents. 1,2-Distearoyl-*sn*-glycero-3-phosphoethanolamine-*N*-[(polyethylene glycol)-2000] (DSPE-PEG2000) was purchased from Avanti Polar Lipids. 1,2-Distearoyl-*sn*-glycero-3-phosphoethanolamine-*N*-[maleimide(polyethylene glycol)-2000] (DSPE-PEG2000-MAL) was purchased from Shanghai Ponsure Biotech. Antibodies targeting human oestrogen receptor (anti-ER, mouse monoclonal) and progesterone receptor (anti-PR, mouse monoclonal) were purchased from Perseus Proteomics. Antibodies targeting human epithelial growth factor receptor-2 (anti-HER2, mouse monoclonal) were purchased from R&D Systems, Bio-Techne. All chemicals were used as received, without further purification.

Nanoparticle synthesis. Core–multi-shell nanoparticles were synthesized using a layer-by-layer protocol. First, to obtain the $NaGdF_4$ core, 2.0 mmol $GdCl_3$, 12.0 ml oleic acid and 30.0 ml ODE were added into a 100 ml flask. The mixture was heated to 140 °C and kept under vacuum for 60 min to form a clear lanthanide-oleate solution. The solution was allowed to cool naturally to 50 °C. A 10 ml volume of methanol containing 5.0 mmol NaOH and 8.0 mmol NH_4F was added, and the mixture was stirred at 50 °C for 60 min. The mixture was then heated to 100 °C and kept for 20 min under vacuum to remove the methanol. The solution was then heated to 280 °C and held for 90 min under a gentle flow of argon to trigger nanocrystal growth, before cooling to room temperature naturally. The produced core nanoparticles were washed twice in ethanol at 7,012 *g* for 5 min, and subsequently dispersed in 20 ml cyclohexane for further use.

The activation shell of $NaGdF_4$:Yb/Ln (Ln = Er, Ho) was then grown epitaxially via hot injection. The shell precursors of $NaGdF_4$:Yb,Ln were prepared following the same procedure as above (the amounts of lanthanide chlorides depending on the composition), until the step where the mixture was heated to 100 °C and kept for 20 min under vacuum to remove the methanol. After that, instead of further heating to 280 °C to trigger nanocrystal growth, the solution was cooled to room temperature to yield the shell precursors. For epitaxial growth, 0.4 mmol of the $NaGdF_4$ core nanoparticles dispersed in 4 ml cyclohexane was added to a 100 ml flask along with 4 ml oleic acid and 6 ml ODE. The mixture was heated to 100 °C and held for 30 min under vacuum, and then heated to 280 °C. The as-prepared shell precursors were injected into the mixture and ripened at 280 °C for 30 min. The resulting nanoparticles were precipitated by the addition of ethanol, collected by centrifugation at 7,012 *g* for 5 min, and washed with ethanol several times before re-dispersal in 4 ml cyclohexane for further use. Different shell thicknesses were obtained by controlling the amount of the shell precursors injected for epitaxial growth. The procedures for further coating the energy relay shell of $NaYF_4$:Yb and the absorption shell of $NaNdF_4$:Yb are as above, except the seeds and shell precursors were consumed. The core–multi-shell nanoparticles of $NaGdF_4$@$NaGdF_4$:Yb/Ln@$NaYF_4$:Yb@$NaNdF_4$:Yb were finally obtained after three stages of epitaxial growth. Details of the synthesized nanoparticles are described in Supplementary Sections 1 and 2.

Characterization instruments. TEM, HRTEM and HAADF-STEM were performed on a JEM-2100F transmission electron microscope with an accelerating voltage of 200 kV equipped with a post-column Gatan imaging filter (GIF-Tri-dium). X-ray diffraction (XRD) measurements were carried out at room temperature on a Bruker D8 diffractometer using Cu Kα radiation (wavelength = 1.5406 Å). Luminescence emission spectra and decay curves were measured on an Edinburgh FLS980 spectroscope equipped with an 808 nm diode laser (MLL-III-808-2W, Changchun New Industries Optoelectronics Tech Co.), with all the as-prepared nanoparticles dispersed in cyclohexane to form transparent colloidal solutions at the same particle concentration of 10 mg ml^{-1}. Absorption spectra were obtained on a PerkinElmer Lambda 750S UV–vis–NIR spectrometer.

Time-resolved NIR-II imaging system. A customized time-gating module was built and coupled to a cooled InGaAs camera (NIRvana: 640, Princeton Instruments; 640 × 512 pixels). The module consists of a camera lens (SWIR-16, Navitar), a focusing lens (f = 20 mm), a high-speed optical chopper (C995, Terahertz Technologies) and a magnifier lens pair (×10 magnification; f_1 = 20 mm and f_2 = 200 mm). The object was placed around 100 mm in front of the camera lens. Excitation was provide by an 808 nm diode laser (D32-21312-112, BWT Beijing, maximum continuous-wave power of 8 W). Emission light collected by the camera lens was passed through a 1 mm pinhole attached in close proximity to the chopper blade, and magnified 10 times to project onto the sensor of the camera. Different filter sets were used to select the emission band of the Ho and Er nanoparticles, respectively. All lenses used were C-coated to maximize transmission for 1,000–1,700 nm. Synchronization was performed by sending the transistor–transistor logic (TTL) signal output from the chopper to a multifunction I/O device (USB-6353, National Instruments), which generated a delayed TTL signal to trigger the excitation laser. A series of time delays were used to acquire signal corresponding to different sections of the luminescence decay curves, allowing lifetime values to be computed for each pixel (for details see Supplementary Sections 3 and 7).

Lifetime coding. PDMS beads were encoded using lifetime-engineered Er and Ho nanoparticles. Assuming tunable ranges of 0–4,000 µs and 0–1,000 µs for the Er^{3+} and Ho^{3+} luminescence lifetime channels, respectively, we can subdivide each into ten sections (for example, evenly separated) and fine-tune the lifetime of a nanoparticle population to be within one particular section. To make a barcode, one population of Er nanoparticles and one population of Ho nanoparticles were selected and added into a solution of PDMS (Sylgard 184, Dow Corning, with curing agent in a 10:1 ratio). After thorough mixing, the composite was degassed under vacuum for 2 h at room temperature. Next, the nanoparticle-containing PDMS was dropped into hemisphere pits (ϕ = 1 mm) of an aluminium mould, heated to 80 °C and kept overnight. The solid PDMS beads were then detached from the mould using a blade. Every single bead thus represented two decimal digits, each corresponding to 0–9. The sequence of the codes was predetermined, for example with the first digit for the Ho^{3+} channel and the second for the Er^{3+} channel. To decode a mixture of encoded beads, time-resolved imaging was performed sequentially at the two emission bands selected by colour filters. The lifetime barcode of each bead was then unambiguously identified based on its lifetime values in the Ho^{3+} and Er^{3+} channels. For more details see Supplementary Section 4.

Antibody conjugation. The oleic-acid-capped Er nanoparticles were transferred to aqueous solution, followed by antibody conjugation through active ester maleimide-mediated coupling between the amine and sulfhydryl. Briefly, 20 mg of oleic-acid-capped Er nanoparticles in chloroform (500 µl) was mixed with a chloroform solution (10 ml) containing 25 mg DSPE-PEG2000 and 2.5 mg DSPE-PEG2000-MAL in a 250 ml flask. The mixture was rotary evaporated quickly at 40 °C under vacuum and kept in vacuum overnight to remove chloroform. The attached film was then hydrated with 5 ml Milli-Q water by vigorous shaking. The colloidal solution was transferred to a microtube, and excess lipids were removed by ultracentrifugation and washing twice. The purified maleimide-conjugated Er nanoparticles were dispersed in 500 µl Milli-Q water. Next, 10 µl of the antibodies at a concentration of ~1 mg ml^{-1} were reduced with 10 mM of tris(2-carboxyethyl) phosphine (TCEP) by shaking for 1 h to expose free sulfhydryls. The reduced antibodies were mixed with the maleimide-conjugated nanoparticles. Finally, the conjugated nanoparticles were purified and collected using ultracentrifugation (105,700 *g*, 10 min, three times). The water-soluble nanoparticles were examined using TEM and dynamic light scattering (Zetasizer Nano, Malvern Instruments), and the stability of their lifetimes was verified using time-resolved NIR-II imaging (Supplementary Section 5).

Animal experiment protocol. Female BALB/c nude mice (6 weeks old, average weight of 20 g) were purchased from Shanghai SLRC Laboratory Animal Centre. All animal procedures were in agreement with the guidelines of the Institutional Animal Care and Use Committee of Fudan University and performed accordingly. MCF-7 and BT-474 cells were obtained from Stem Cell Bank, Chinese Academy of Sciences. The cells were authenticated by a short tandem repeat test, and confirmed free of mycoplasma contamination using a mycoplasma detection kit. To obtain tumours, 5×10^5 tumour cells (either MCF-7 or BT-474) were seeded in each cell culture flask containing 8 ml of Gibco RPMI 1640 medium supplemented with 10% FBS and 1% antibiotics, and incubated in CO_2 for 24 h at 37 °C. The tumour cells were harvested by centrifugation and resuspended in sterile PBS, and implanted subcutaneously into the right fore legs of five-week-old mice (5×10^7 cells per mouse). When the tumours reached 5 mm in diameter (14 days after implantation), the mice were killed and the tumours were taken out, sheared into tissue blocks (1 mm × 1 mm × 1 mm) and resuspended in sterile PBS. The tumour blocks were implanted subcutaneously into the dorsum of the nude mice. When the tumour reached ~4–6 mm in diameter (~10–11 days after implant), the tumour-bearing mice were subjected to imaging studies. PBS solutions of antibody-conjugated Er nanoparticles (5 mg ml^{-1}, 50 µl each) were mixed and intravenously injected through the tail vein for the lifetime imaging experiment. Solutions of DSPE-PEG2000-coated Er nanoparticles were used for the control group. All mice were anaesthetized before imaging. Experimental parameters for imaging are summarized in Supplementary Table 7.

Western blot and IHC assays. For western blot, MCF-7 and BT-474 cell extracts were prepared using a RIPA kit (Shanghai Bogoo Biotechnology). Cell extracts and separate proteins were loaded onto an SDS polyacrylamide gel. The electrophoresed proteins were transferred onto a 0.45 µm nitrocellulose filter membrane and incubated for 30 min at room temperature in 3% BSA–TBST blocking solution. The membrane was then washed at room temperature with TBST five times, followed by incubation overnight at 4 °C in blocking buffer

containing primary antibodies. Next, the membrane was washed with TBST five times, and incubated at room temperature for 40 min in buffer containing a secondary reagent goat anti-mouse-IgG (H+L) horseradish peroxidase (HRP) at 1:10,000. Finally, after washing the membrane at room temperature six times with TBST buffer, the biomarkers were detected based on banding colouration using chemiluminescence reagents. To obtain the semi-quantitative expressions of the biomarkers, the intensity of the optical density (IOD) of the samples was analysed by Image-Pro Plus.

For the IHC test, tumour-bearing mice were killed and all the tumours were collected and then fixed using 4% paraformaldehyde in PBS (pH 7.4) for 30 min at room temperature. The paraformaldehyde solution was removed by rinsing the tumour tissue three times in PBS, and the cells were permeabilized using 0.3% Triton X-100 in PBS for 15 min, followed by rinsing three times with PBS. Next, 0.3% H_2O_2-methanol solution was added, and after incubation for 10 min, removed by rinsing three times with PBS. To block non-specific hybridization, 2% BSA in PBS was added to incubate the tissues for 30 min at 37 °C. ER, PR and HER2 antibodies were added separately to the tissues on coverslips, followed by S28 (antibody response enhancer), and incubated for 1 h at 37 °C. The incubating solution was then removed by rinsing three times for 5 min with PBS. All cover lips were incubated with a dilution of HRP-labelled secondary antibody in PBS and 2% BSA for 30 min at 37 °C, followed by rinsing four times for 5 min with PBS, and immersed in freshly prepared DAB solution. The tissues were counterstained in haematoxylin for 5 min, then rinsed twice with tap water. Each coverslip was placed with the tissues down onto a glass slide containing a drop of mounting medium, followed by microscopy examination (Olympus BX53). For a detailed analysis of the IHC images see Supplementary Section 8.

Reporting summary. Further information on experimental design is available in the Nature Research Reporting Summary linked to this article.

Data availability. The data that support the plots within this paper and other findings of this study are available from the corresponding authors upon reasonable request.

nature research

Corresponding author(s): Fan Zhang, Yiqing Lu

Reporting Summary

Nature Research wishes to improve the reproducibility of the work that we publish. This form provides structure for consistency and transparency in reporting. For further information on Nature Research policies, see Authors & Referees and the Editorial Policy Checklist.

Statistical parameters

When statistical analyses are reported, confirm that the following items are present in the relevant location (e.g. figure legend, table legend, main text, or Methods section).

n/a	Confirmed	
☐	☒	The exact sample size (*n*) for each experimental group/condition, given as a discrete number and unit of measurement
☐	☒	An indication of whether measurements were taken from distinct samples or whether the same sample was measured repeatedly
☒	☐	The statistical test(s) used AND whether they are one- or two-sided *Only common tests should be described solely by name; describe more complex techniques in the Methods section.*
☒	☐	A description of all covariates tested
☒	☐	A description of any assumptions or corrections, such as tests of normality and adjustment for multiple comparisons
☐	☒	A full description of the statistics including central tendency (e.g. means) or other basic estimates (e.g. regression coefficient) AND variation (e.g. standard deviation) or associated estimates of uncertainty (e.g. confidence intervals)
☒	☐	For null hypothesis testing, the test statistic (e.g. *F*, *t*, *r*) with confidence intervals, effect sizes, degrees of freedom and *P* value noted *Give P values as exact values whenever suitable.*
☒	☐	For Bayesian analysis, information on the choice of priors and Markov chain Monte Carlo settings
☒	☐	For hierarchical and complex designs, identification of the appropriate level for tests and full reporting of outcomes
☒	☐	Estimates of effect sizes (e.g. Cohen's *d*, Pearson's *r*), indicating how they were calculated
☐	☒	Clearly defined error bars *State explicitly what error bars represent (e.g. SD, SE, CI)*

Our web collection on statistics for biologists may be useful.

Software and code

Policy information about availability of computer code

Data collection	A LabVIEW program was used to control the purpose-built time-resolved NIR-II imaging system and acquire the lifetime images.
Data analysis	MATLAB codes were used to analyse the lifetime-multiplexed images and the immunohistochemistry images, according to the methods described in Supplementary Information SI-7 and SI-8, respectively. Image-Pro Plus was used to analyse the western plot data.

For manuscripts utilizing custom algorithms or software that are central to the research but not yet described in published literature, software must be made available to editors/reviewers upon request. We strongly encourage code deposition in a community repository (e.g. GitHub). See the Nature Research guidelines for submitting code & software for further information.

Data

Policy information about availability of data

All manuscripts must include a data availability statement. This statement should provide the following information, where applicable:

- Accession codes, unique identifiers, or web links for publicly available datasets
- A list of figures that have associated raw data
- A description of any restrictions on data availability

The data that support the plots within this paper and other findings of this study are available from the corresponding authors upon reasonable request.

Field-specific reporting

Please select the best fit for your research. If you are not sure, read the appropriate sections before making your selection.

☒ Life sciences ☐ Behavioural & social sciences ☐ Ecological, evolutionary & environmental sciences

For a reference copy of the document with all sections, see nature.com/authors/policies/ReportingSummary-flat.pdf

Life sciences study design

All studies must disclose on these points even when the disclosure is negative.

Sample size	No sample size calculations were performed. The sample size (n) of each experiment is provided in the corresponding figure captions in the paper and supplementary information. Sample sizes were chosen to support meaningful conclusions.
Data exclusions	No data were excluded from the analyses.
Replication	Animal experiments were performed on biological replicates following identical procedures to verify the reproducibility of the experimental findings.
Randomization	The tumour-bearing mice were randomly allocated into the positive and control groups.
Blinding	Investigators were not blinded to group allocation during data collection and analysis, due to limited personnel.

Reporting for specific materials, systems and methods

Materials & experimental systems

n/a	Involved in the study
☒	☐ Unique biological materials
☐	☒ Antibodies
☐	☒ Eukaryotic cell lines
☒	☐ Palaeontology
☐	☒ Animals and other organisms
☒	☐ Human research participants

Methods

n/a	Involved in the study
☒	☐ ChIP-seq
☒	☐ Flow cytometry
☒	☐ MRI-based neuroimaging

Antibodies

Antibodies used	Monoclonal human ER alpha antibody (Catalog # PP-H4624-00, Clone # H4624, Lot # A-2) and human PR common antibody (Catalog # PP-A9621A-00, Clone # A9621A, Lot # A-1) were purchased from Perseus Proteomics. Monoclonal human ErbB2/Her2 antibody (Catalog # MAB1129-100, Clone # 191924, Lot # IBD0716121) was purchased from R&D Systems, Bio-Techne.
Validation	Validation details of the primary antibodies are available on the manufacturers' websites: http://www.ppmx.com/en/products/antibody/NuclearReceptor/er-alpha_H4624.html http://www.ppmx.com/en/products/antibody/NuclearReceptor/pr-common_A9621A.html https://www.rndsystems.com/cn/products/human-erbb2-her2-antibody-191924_mab1129

Eukaryotic cell lines

Policy information about cell lines

Cell line source(s)	MCF-7 and BT-474 cell lines were obtained from Stem Cell Bank, Chinese Academy of Sciences (Shanghai, China).
Authentication	All cell lines were authenticated by Short Tandem Repeat test.
Mycoplasma contamination	All cell lines tested negative for mycoplasma contamination.
Commonly misidentified lines (See ICLAC register)	No commonly misidentified cell lines were used in the study.

Animals and other organisms

Policy information about studies involving animals; ARRIVE guidelines recommended for reporting animal research

Laboratory animals	Female Balb/c nude mice (6 weeks old) were obtained from Shanghai SLRC Laboratory Animal Centre (China).
Wild animals	The study did not involve wild animals.
Field-collected samples	The study did not involve sampled collected from the field.